

Leading Edge Vortex Development on a Waving Wing at Reynolds Numbers Between 10,000 and 60,000

Anya R. Jones* and Holger Babinsky†

University of Cambridge, Cambridge CB2 1PZ, United Kingdom

The waving wing experiment is a fully three-dimensional simplification of the flapping wing motion observed in nature in which the spanwise velocity gradient and wing starting and stopping acceleration that exist on an insect-like flapping wing are generated by rotational motion of a finite span wing. The flow development around a waving wing at Reynolds numbers 10,000, 30,000, and 60,000 was studied using high speed PIV to capture the unsteady velocity field. Vorticity fields were computed and a vortex detection algorithm implemented in order to identify individual vortices in the flow. Vortex development was quantified by computing the circulation of the leading edge vortex as a function of time. The leading edge vortex was found to develop more quickly (in a non-dimensional time) at lower Reynolds numbers. Lift and drag forces were measured using a two-component force balance. The lift curve shape was similar at all of the Reynolds numbers tested. A transient high lift peak approximately 1.5 times the quasi-steady value occurred in the first chord-length of travel, caused by the formation of a strong attached leading edge vortex. Although the shape of the curve was similar, the timing of the transient lift peak varied with Reynolds number. The maximum lift at a Reynolds number of 30,000 occurred at a stroke angle of approximately $\theta = 3.6$ deg, but at a Reynolds number of 60,000 the lift peak occurred at $\theta = 7.4$ deg. Although Reynolds number was not found to affect the fundamental structure of the flow development, but it can affect the time-scale of the development of flow structures and thus the lift force produced.

Nomenclature

c	Wing chord	θ	Wing stroke angle
U	Local wing speed	ω	Vorticity or Angular velocity
U_∞	Target wing speed at 3/4 span, $Re\nu/c$	AR	Aspect ratio
x	Distance traveled	C_L	Coefficient of lift
α	Angle of attack, deg	Re	Reynolds number based on velocity at 3/4 span
Γ	Circulation	Ro	Rossby number
Γ^*	Normalized circulation, $\Gamma/U_\infty c$		

I. Introduction

EFFORTS to develop micro air vehicles (MAVs) have renewed interest in unsteady low Reynolds number aerodynamics. MAVs are by definition small vehicles with a low cruise speed and a target endurance of about an hour. The primary driver for MAV development is reconnaissance, a mission that requires both endurance and maneuverability in a flight regime that is still largely unexplored. At MAV-like Reynolds numbers, generating sufficient lift can be difficult and engineers have turned to biology for inspiration. MAVs have mission requirements not dissimilar from natural fliers like birds and insects, both of which are more

*Assistant Professor, University of Maryland, Department of Aerospace Engineering, 3154 Glenn L. Martin Hall, College Park, MD 20742, AIAA Member.

†Professor, University of Cambridge, Department of Engineering, Trumpington Street, Cambridge CB2 1PZ, United Kingdom, AIAA Member.

maneuverable and efficient than current MAV designs. Zoologists have long studied natural flight and have produced a large amount of data regarding the wing kinematics, sizes, and flight speeds for a wide range of flying creatures. The flow patterns observed are, however, highly complex and there is still a lot to learn about lift generation in this flight regime.

The primary source of lift on insect wings was identified by Ellington et al.¹ Smoke flow visualizations on a dynamically scaled hawkmoth wing revealed the formation of a spiral vortex along the leading edge of the wing that persisted through the downstroke at Reynolds numbers near 2,000. An attached leading edge vortex has since been observed by multiple research groups on both mechanical wing flappers^{1–4} and simplified models,⁵ though some researchers have also observed unstable leading edge vortices that shed from the wing.^{6–8}

In order to form a stable attached leading edge vortex there must be some stabilizing force. In early experiments on a mechanical wing flapper at $Re = 2,000$ Ellington et al.¹ observed a spanwise flow of the same order as the wing tip speed. The presence of such a flow could stabilize the leading edge vortex much like on a delta wing, by transporting vorticity towards the wing tip and limiting the growth of the vortex.^{1,3,4,9} At lower Reynolds numbers, the spanwise flow is not nearly as strong.¹⁰ Birch et al.² report that at $Re = 120$ spanwise flow does exist but is of a much lower velocity than at Reynolds numbers $O(1,000)$ and that at this lower Reynolds number spanwise flow is strongest behind the leading edge vortex rather than at the vortex core. At Reynolds numbers $O(100)$ spanwise flow exists both within the core of the leading edge vortex and behind it, but is relatively weak. Thus if the leading edge vortex stability is related to the strength of the spanwise flow along the wing, Reynolds number could play a critical role in the development of lift-generating flow structures.

At higher Reynolds numbers $O(1,000)$ the structure of the leading edge vortex may be more sensitive to the conditions. Ellington et al.¹ and Birch et al.² both performed experiments at similar Reynolds numbers, $Re = 2,000$ and $1,400$ respectively. Both sets of experiments on mechanical wing flappers reveal a stable attached spiral leading edge vortex. Later experiments by Lentink and Dickinson⁷ demonstrate a spiral vortex in which the core bursts, forming a less coherent region of recirculating flow that remains attached to the wing. At a Reynolds number of 8,000 Tarascio et al.⁶ observed vortices periodically shedding from a flapping wing.

The waving wing experiment is a fully three-dimensional simplification of the flapping wing motion observed in nature and mimicked by the mechanical wing flappers mentioned above. The spanwise velocity gradient that exists on an insect-like flapping wing is generated by rotational motion of a finite span wing in a manner similar to revolving wing experiments.⁵ Waving wing experiments also preserve wing starting and stopping acceleration which is likely to be significant over a short wing stroke. This setup preserves key features of the wing stroke which are neglected in other models while the simple geometry allows identification of fundamental structures in the flow.

Previous waving wing experiments were performed at a Reynolds number of 60,000. This is at the high end for the current generation of micro air vehicle designed and as MAVs continue to get smaller, so will the operating Reynolds number. As the Reynolds number drops, transition may affect vortex development and lift generation and an understanding of Reynolds number effects is important for two reasons. First, there is a large body of work performed by zoologists at very low Reynolds numbers $O(100)$ and it is useful to relate current engineering low Reynolds number research typically at $Re = O(1,000 – 10,000)$ to previous findings. Secondly, it is crucial for MAV design to know if a “critical” Reynolds number exists for the effects previously observed on the waving wing, namely the development of an unstable leading edge vortex responsible for a high lift transient.

II. Experimental Methods

A. Experimental Setup and Measurement Techniques

Experiments were conducted by waving a flat plate wing through a tank filled with water. Using water as the working medium, it is possible to achieve the required Reynolds numbers with relatively slow motions, allowing for very high temporal resolution while at the same time providing an optimal environment for force measurements and optical flow diagnostics. A sketch and photo of the waving mechanism is shown in Figure 1. The waving motion is controlled by a servomotor and gearbox programmable through LabView. A force balance can be mounted on the wing to provide unsteady lift and drag force measurements. The angle of attack is selectable from 0 to 45 degrees in 5 degree increments. The wing is a 2.5% thick carbon fiber flat

plate with rounded edges, a chord of 0.125 m, an aspect ratio of 4, and a Rossby number of 4.4. The wing stroke is a linear velocity profile in time with constant angular acceleration over a stroke angle of 4 degrees (0.25 chord-lengths of travel at the 3/4 span reference plane) to the target velocity, $U_\infty = \text{Re} \nu/c$. The wing decelerated in the same way before reaching a maximum stroke angle of 90 degrees.

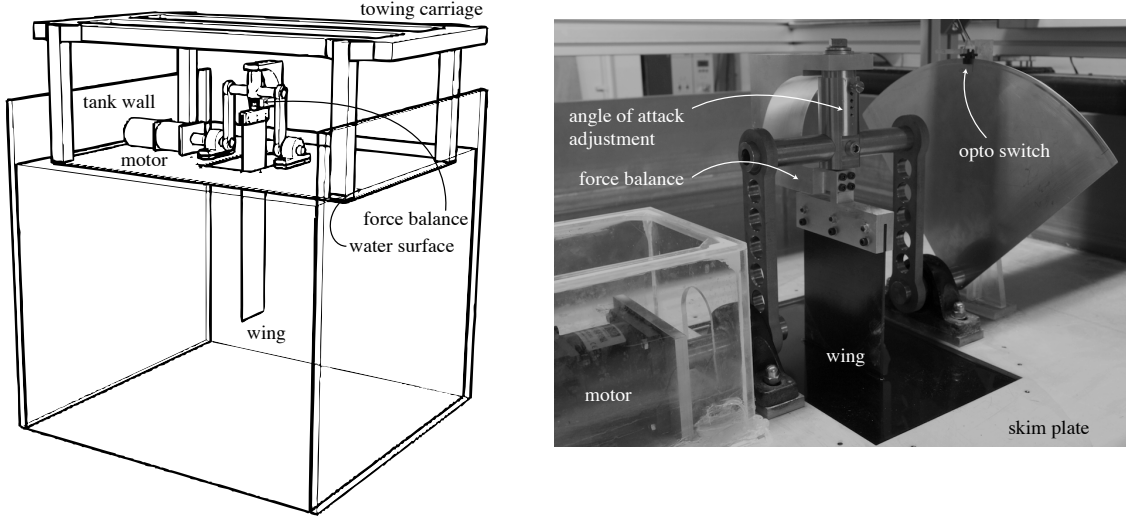


Figure 1. The waving wing mechanism.

Two-component force balance measurements were taken in both air and water at 7 kHz. Wing lift and drag coefficients were obtained by subtracting the inertial forces measured in air from the forces measured in water and normalizing by the local wing velocity such that $C_L = 6L/[\rho\omega^2 c(r_t^3 - r_r^3)]$ where r_t and r_r are the distances from the axis of rotation to the wing tip and wing root. Force data was averaged over five runs.

Particle image velocimetry was performed using a LaVision FlowMaster 4S DPIV with a high resolution high speed camera. To obtain PIV data for chordwise slices of the waving wing, a horizontal laser sheet entered the tank through the side wall and the camera was placed below the tank as shown in Figure 2. PIV images were taken at frame rates between 50 and 750 Hz at a resolution of 1024×1024 pixels with a 20×20 cm or 35×35 cm field of view. Frame rates were chosen for a 3 to 5 pixel particle displacement within image pairs. The average velocity field was obtained by averaging the velocity components at each spatial point across 5 runs. Further details on the experimental setup, wing kinematics, and measurement techniques can be found in References 8 and 11.

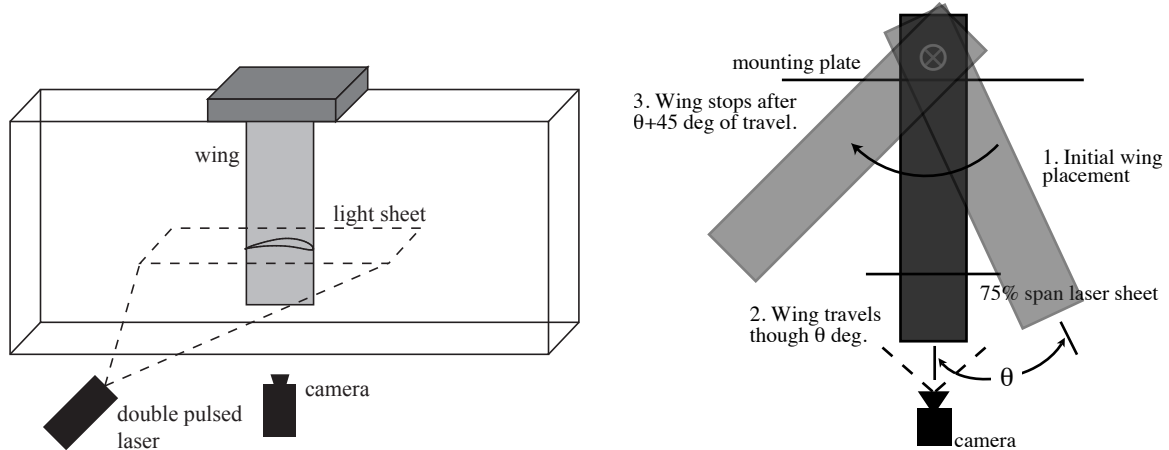


Figure 2. Chordwise PIV setup.

B. Experimental Uncertainty

The wing angle of attack is accurate to within 1/60 of a degree and the position to within 0.2 degrees or 0.06 mm at 3/4 span. The wing position as a function of time was measured using a high speed camera at 2 kHz and the angular position of the wing computed for three runs at $Re = 60,000$ and a 45 degree angle of attack, a particularly taxing case for the servo motor. Once the wing has reached its constant velocity there is a 10% error in position or a 3.5% error in angular velocity. The relatively large error in wing position appears to be due to a slight delay in the start of the wing motion. Error in the wing velocity is much lower.

Forces acting on the wing produce a significant bending moment at the balance because the force balance is mounted at the wing root. A moment correction was determined by estimating the center of force on the wing (assuming a constant force coefficient) and computing the quasi-steady moment applied to the force balance in each channel. The correction is approximately a -9% change in the lift coefficient and a +6% change in the drag coefficient for an aspect ratio 4 wing at a 35 degree angle of attack. The RMS and bias error for both the force signal and the force coefficient are given in Table 1. The RMS of the force signal is of the same order of magnitude at all three Reynolds numbers but when normalized by the flow speed, the RMS of the force coefficient at $Re = 10,000$ is an order of magnitude larger than the RMS at $Re = 60,000$ and approximately 5 times larger than that at $Re = 30,000$. Due to the relatively high error, the force data taken at a Reynolds number of 10,000 will not be presented here. Even at $Re = 30,000$ the error in the force coefficient is high and at low angles of attack the signal to noise ratio is low.

Table 1. Uncertainty in Force Measurements.

	Force, N		Force Coefficient	
	Ch. 1	Ch. 2	Ch. 1	Ch. 2
Re = 60,000				
RMS	0.41	0.81	0.09	0.18
Bias error	0.10	0.06	0.02	0.01
Re = 30,000				
RMS	0.56	0.43	0.51	0.39
Bias error	-0.04	0.01	-0.04	0.01
Re = 10,000				
RMS	0.32	0.26	2.35	2.38
Bias error	0.04	-0.05	0.45	-0.23

Some of the force data presented here is shown as a smoothed curve for clarity. A moving average over 400 samples of 0.06 s was applied to the raw force signal. Approaching the ends of the signal, the averaging window shrinks and errors can be larger in those regions, but in general the smoothed signal preserves the shape of the curves well and makes comparisons much clearer. Examples of the unsteady lift and drag coefficients at a 25 degree angle of attack is given in Figure 3 for $Re = 30,000$ and $60,000$. The raw data is shown in grey and smoothed signal is given by the solid black line. Error bars represent the RMS error in the force coefficients. At both Reynolds numbers there is steep lift peak very early on in both the raw and the smoothed signal as well as a dip due to inertial forces near the end of the stroke. The force peaks are much larger in the raw signal than in the smoothed and it is impossible to tell if this is due to vibration or an aerodynamic force, but the difference in magnitude of the lift peak is within the experimental error.

C. Analysis Techniques

1. Vortex Detection

Velocity fields obtained through PIV provide useful information, but it can be difficult to detect and track vortices in both time and space though a complex velocity field as expected on the waving wing. In particular, a leading edge vortex is expected to form and the behavior of this vortex is of primary interest. In order to gain a better understanding of the flow physics, the velocity fields measured using PIV were analyzed using two vortex detection methods.

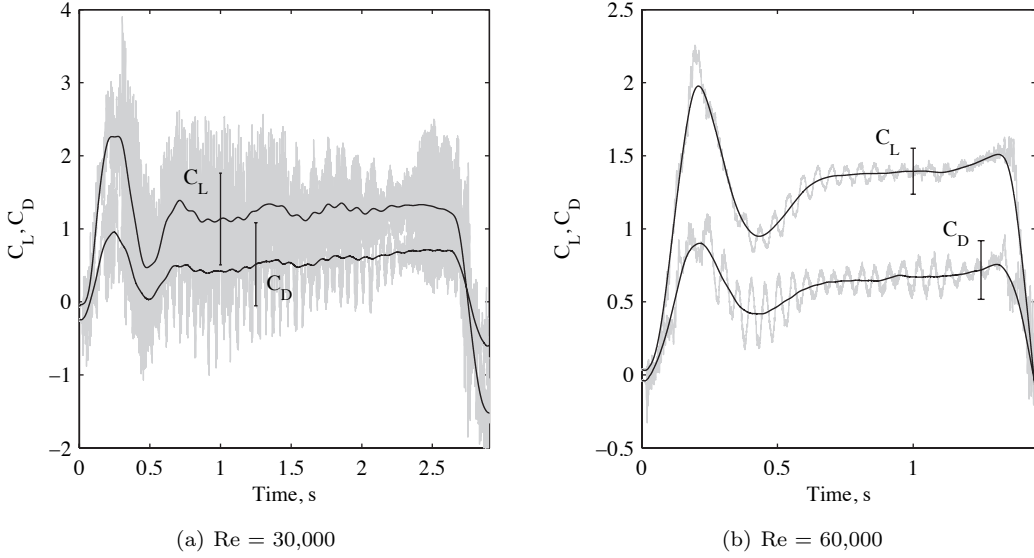


Figure 3. Force coefficients at $\alpha = 25$ deg.

VORTICITY FIELD The most common way of detecting vortices in a flow is to directly compute the vorticity field by taking the curl of the velocity field and an area of the flow field with a high vorticity value can be considered a vortex. This method is straightforward but presents two difficulties. First, differentiating the velocity measurements amplifies noise in the PIV data. Secondly, since the magnitude of the vorticity in a shear layer and vortex can be comparable, it can be difficult to identify vortices in a shear flow.¹²

The central differencing scheme $\left(\frac{df}{dx}\right)_i \approx \frac{f_{i+1} - f_{i-1}}{2\Delta x}$ is accurate to $O(\Delta x)$. The truncation uncertainty is $\epsilon_t \approx 0.7\epsilon/\Delta x$ where ϵ is the uncertainty in the velocity measurements and Δx is a function of the resolution of the velocity field.¹³ The uncertainty in the velocity measurements is $\epsilon_m \approx \sqrt{\epsilon_u^2 + \epsilon_v^2}$ where ϵ_u is the error in the velocity measurements \pm in m s^{-1} divided by Δx and ϵ_v is assumed to be approximately equal to ϵ_u . The square of the total error ϵ_ω in the vorticity computations is the sum of the squares of the truncation error ϵ_t and the measurement error ϵ_m . Values are given in Table 2. To make it easier to compare the flow-field at different locations on the wing at different Reynolds numbers, the vorticity fields given here show only the data outside of the error and have been non-dimensionalized by the local wing speed and wing chord such that $\omega^* = \omega/(U_\infty c)$.

Table 2. Uncertainty in the computation of the vorticity field.

	Re = 60,000		Re = 30,000		Re = 10,000	
Field of view, cm	20 × 20	35 × 35	20 × 20	35 × 35	20 × 20	35 × 35
$\epsilon_t, \text{s}^{-1}$	3.7	2.1	1.8	1.0	0.6	0.4
$\epsilon_u, \epsilon_v, \text{s}^{-1}$	5.2	3.0	2.6	1.5	0.9	0.5
$\epsilon_m, \text{s}^{-1}$	7.4	4.2	3.7	2.1	1.2	0.7
$\epsilon_\omega, \text{s}^{-1}$	8.3	4.7	4.1	2.3	1.3	0.8

γ FIELD Vorticity can be considered a local vortex detection scheme in which calculations are performed at individual points in the flow field to determine if they belong to a vortical structure. Non-local schemes also exist in which the flow surrounding the point in question is considered. One such algorithm developed by Graftieaux et al.¹⁴ considers the topology of the velocity field rather than the magnitude and therefore reliably detects vortices of any strength as long as they exhibit a coherent swirling pattern. A scalar function

[†]The total error for the PIV measurements, $\epsilon_{tot} = \epsilon_{bias} + \epsilon_{rms}$ is near $+0.03/-0.05$ pixels. Calibration error is approximately 0.2 pixels and the total error at $Re = 30,000$ is approximately 0.029 ms^{-1} .

γ at point P is defined as

$$\gamma(P) = \frac{1}{N} \sum_S \sin(\theta_M)$$

where S is a two-dimensional area centered on point P and N is the number of points inside S . θ_M is the angle between the radius vector from P to a point M that lies on S and the relative velocity vector at M , the total velocity at the point M minus the average velocity across the area S . γ is at its maximum when P is at the center of an axisymmetric vortex and is a measure of the vortex strength.¹⁴

This vortex detection algorithm is largely independent of the domain size, but the values of γ in the flow field are slightly sensitive to the size of the area S . Figure 4 shows contours of the γ -field for $|\gamma| \geq 0.6$ in increments of 0.1 for three different sizes of S . Red contours represent positive values of γ and vortices rotating clockwise. Blue contours represent negative values of γ and vortices rotating counterclockwise. When the area of S is very small there is a significant amount of noise in the γ -field. When the area of S is very large, the γ -field does not resolve very small vortices. A domain size of $S = 7 \times 7$ vectors was selected, representing an area of 10.94 mm^2 in the flow field.

Because the computation of γ relies on a domain S , values of γ can be dependent on the resolution of the velocity field. If a vortex core does not have a diameter greater than S the value of γ at a given point in the vortex core may be artificially low if the data resolution is low. This issue does not affect vortex detection, but does become a consideration when γ -contours are used for some quantitative analyses as discussed in Sections 2 and 3 below.

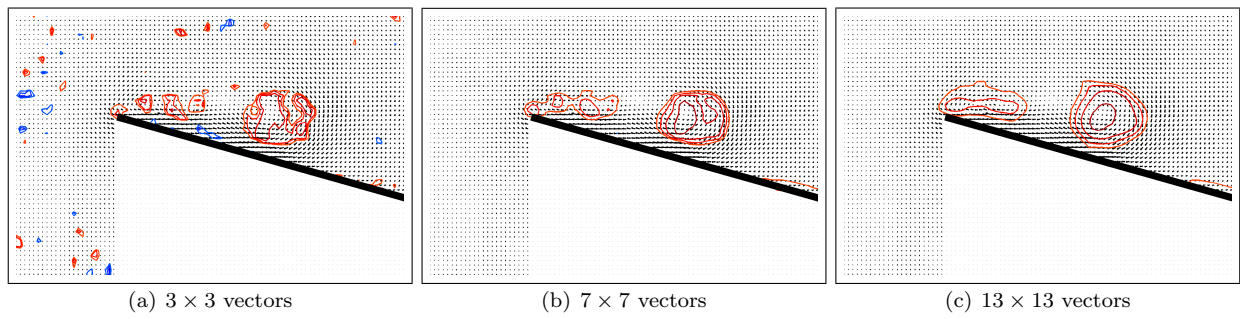


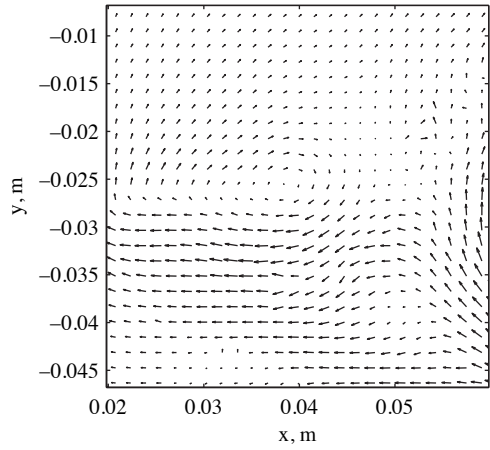
Figure 4. Sensitivity of the γ -field to domain size.

2. Vortex circulation

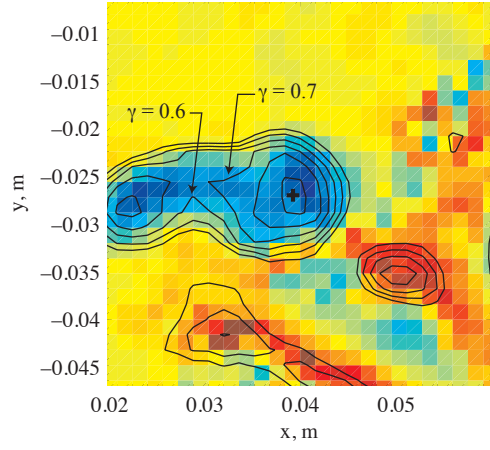
The circulation of a vortex can be computed from the velocity field by first computing the vorticity field $\omega = \nabla \times \mathbf{u}$ and then integrating $\Gamma = \int \omega \cdot dS$ over the vortex core. An example of a typical flow field on the waving wing is shown in Figure 5. It is difficult to identify the vortices in the velocity field, but the vorticity and γ fields reveal multiple vortices very near each other and a region of high vorticity between them. The circulation Γ of the vortex marked with a + was computed by integrating around contours of γ between 0.4 and 0.8. The results (Figure 6) show that the value of the vortex circulation is a function of the path of integration. High γ -contours may exclude some of the vortex core and low γ -contours may surround multiple vortices (as illustrated in Figure 5(b)), resulting in artificially high circulation values. A 16% increase in the $\gamma = 0.6$ contour of integration to $\gamma = 0.7$ results in a 68% change in the circulation value. Since there is no definite “correct” path of integration the numerical value of the circulation is not very useful. However, given the time-resolved velocity fields measured using PIV and the tracking method described above, the circulation of a vortex can be shown as a function of time. Figure 7 shows the vortex circulation as computed using three different γ -contours as the path of integration. Although the numerical value of Γ depends on the integration path, the shape of the Γ versus time curve does not. This analysis provides useful information regarding the rate of change of vortex circulation and can be used to quantify vortex growth.

3. Vortex break-off

In a typical flow over the waving wing, flow separates at the sharp leading edge forming a shear layer. As vorticity is continuously generated at the leading edge, this shear layer grows and discrete vortices break off



(a) Velocity field



(b) Vorticity field and contours of γ

Figure 5. Vortex circulation.

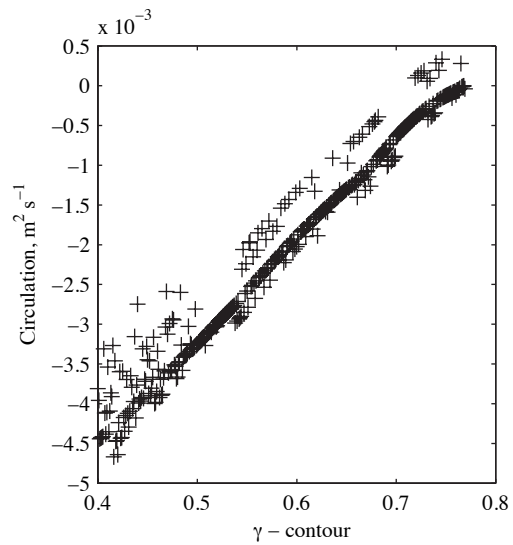


Figure 6. Variation of Γ with path of integration.

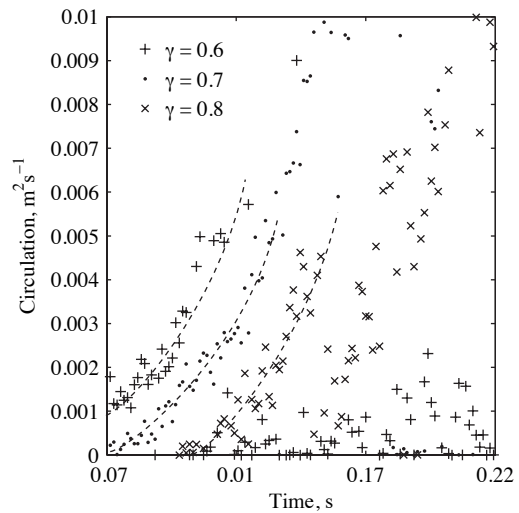
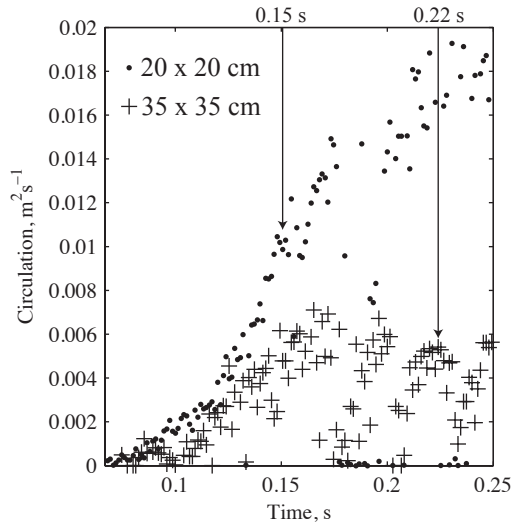
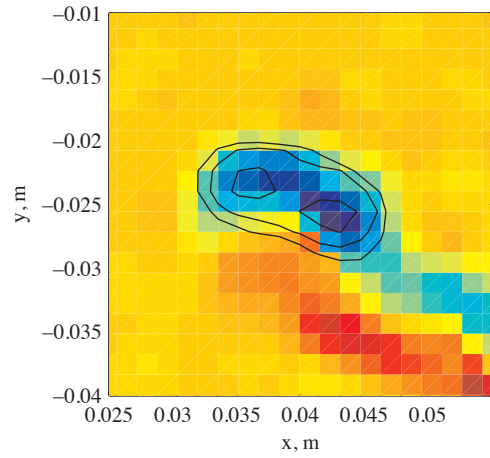


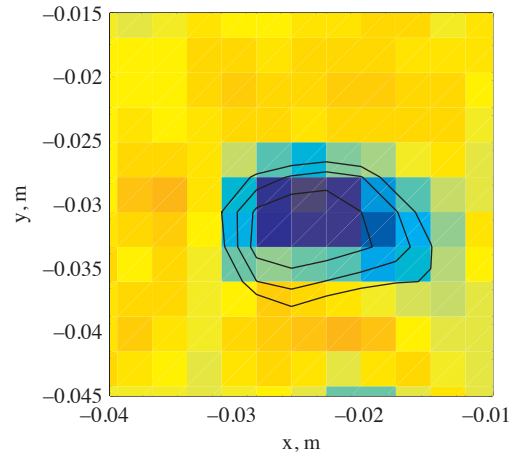
Figure 7. Vortex circulation as a function of time.



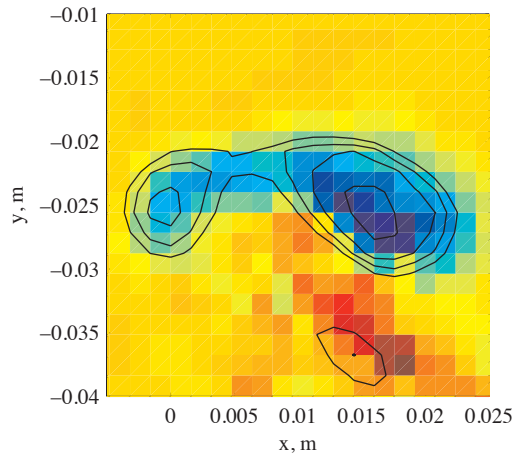
(a) Circulation as a function of time.



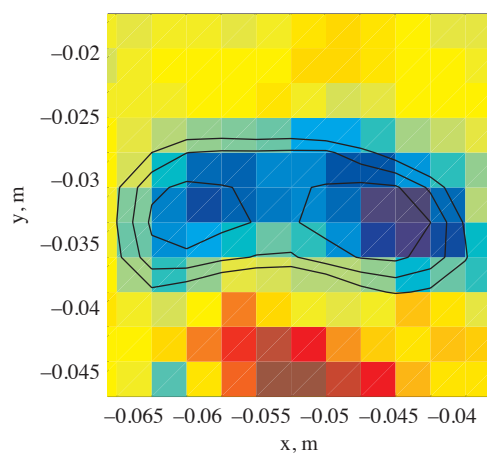
(b) $t = 0.15 \text{ s}, 20 \times 20 \text{ cm}$



(c) $t = 0.15 \text{ s}, 35 \times 35 \text{ cm}$



(d) $t = 0.22 \text{ s}, 20 \times 20 \text{ cm}$



(e) $t = 0.22 \text{ s}, 35 \times 35 \text{ cm}$

Figure 8. Vortex break-off.

and convect downstream. The time-resolved PIV data reveals a trail of vortices shedding from the leading edge and the time at which these vortices separate from the leading edge is of primary interest. Vortex break-off (or shedding) occurs when a region of vorticity splits into two vortex cores. In practice, the $|\gamma| = 0.6$ contour used by Graftieaux et al. to define the vortex core often encloses two smaller cores of higher vorticity and the break-off point is defined here as the point at which two separate regions of $|\gamma| = 0.8$ appear.

The vortex break-off point is highly sensitive to the resolution of the velocity data. Figure 8 shows the vortex circulation as a function of time for two different data sets corresponding to the two resolutions of PIV data. Vortex break-off occurs at $t = 0.15$ s in the higher resolution data and $t = 0.22$ s in the lower resolution data. Snapshots of the vorticity field and γ -contours are given at both break-off times. At $t = 0.15$ s there are clearly two separate $|\gamma| = 0.8$ cores in the high resolution data, but these are not resolved in the low resolution data until $t = 0.22$ s. This time delay represents 4.5 degrees of rotation or 0.25 chord-lengths of travel. Due to this high level of uncertainty, the vortex break-off point for data taken at different resolutions is not comparable.

III. Results and Discussion

A. Flow Over a Waving Wing

The results of previous waving wing experiments,^{8,15} performed at a Reynolds number of 60,000, suggested that the flow on a waving wing develops over three stages as illustrated in Figure 9. At the start of the wing stroke, during the initial *transient*, the flow field is characterized by the growth of a strong leading edge vortex. Flow separates at the sharp leading edge and quickly forms a leading edge vortex which remains attached to the wing. During this phase the strengthening of the leading edge vortex causes a rapid increase in lift. This phase ends when the vortex sheds, moves away from the leading edge, and a second vortex begins to form at the leading edge.

The next flow observed on the waving wing is the *developing flow*. Flow continues to separate over the leading edge and a second leading edge vortex forms. Because the first vortex has moved downstream its effect on lift is diminished. The new leading edge vortex does not achieve the same ultimate strength before it sheds and in this phase the total lift is relatively low.

Finally, in the *established flow* phase a periodic pattern of vortex shedding from the leading edge is observed. During this phase there are multiple vortices present above the wing at all times producing a constant lift coefficient of an intermediate value.

B. Vorticity Fields

Figure 10 shows the flow field at 3/4 span of the waving wing at four points in the wing stroke for a Reynolds number of 60,000 and a 25 degree angle of attack. The colors represent the vorticity in the flow field normalized by the wing chord and the local wing velocity, $\omega^* = \omega/U_\infty c$. The black contours represent contours of a constant $|\gamma| \geq 0.6$. At $Re = 60,000$, maximum lift occurs at $x/c = 0.52$, before the flow field given in (a). The developing flow in which the vortices begin moving downstream over the wing is shown in (b) and the established flow in (d).

Figures 11 and 12 show snapshots of the flow field at Reynolds numbers 30,000 and 10,000 at the same points in the wing stroke. There is more noise in the signal at the lower Reynolds numbers, but vortices are still clearly visible in the flow. In both cases there are multiple vortices visible as early as $x/c = 0.65$ as shown in (a) at which point the initial leading edge vortex has shed and a second has begun to form. Vortices continue to form at the leading edge and as at $Re = 60,000$, the trail of shed vortices reaches the trailing edge at about 40.00 degrees of rotation. The fundamental structure of the flow does not appear to change at Reynolds numbers 10,000 and 30,000 and the flow development follows the same progression as previously observed at a Reynolds number of 60,000.

In Figure 13, the flow field is given at a single point in the wing stroke ($x/c = 0.65$ or $\theta = 10.85$ deg) at Reynolds numbers 10,000, 30,000, and 60,000 with the leading edge of the wing in line. The dashed lines mark the leading edge of the wing and the center of the vortex core at each Reynolds number. The values $d_{10} = 0.25c$, $d_{30} = 0.19c$, and $d_{60} = 0.13c$ give the number of chord-lengths from the leading edge of the wing to the center of the first shed vortex for each Reynolds number tested. It is evident that the distance d increases as Reynolds number decreases, suggesting that the flow develops more quickly (in terms of chord-lengths traveled) and the initial leading edge vortex sheds more quickly at lower Reynolds numbers.

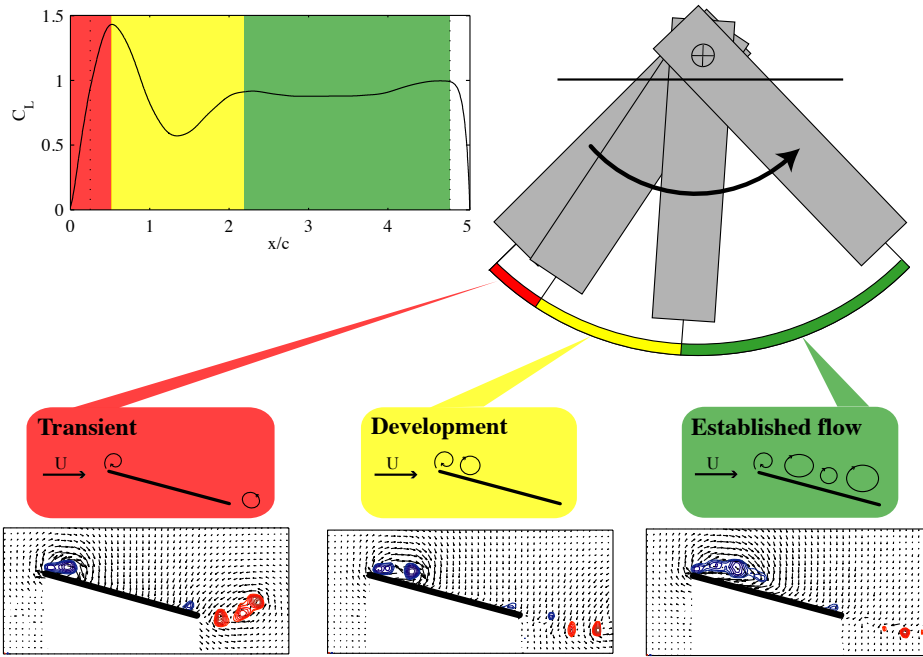


Figure 9. The three stages of flow development on an impulsively started waving wing: Transient, Development, and Established flow.

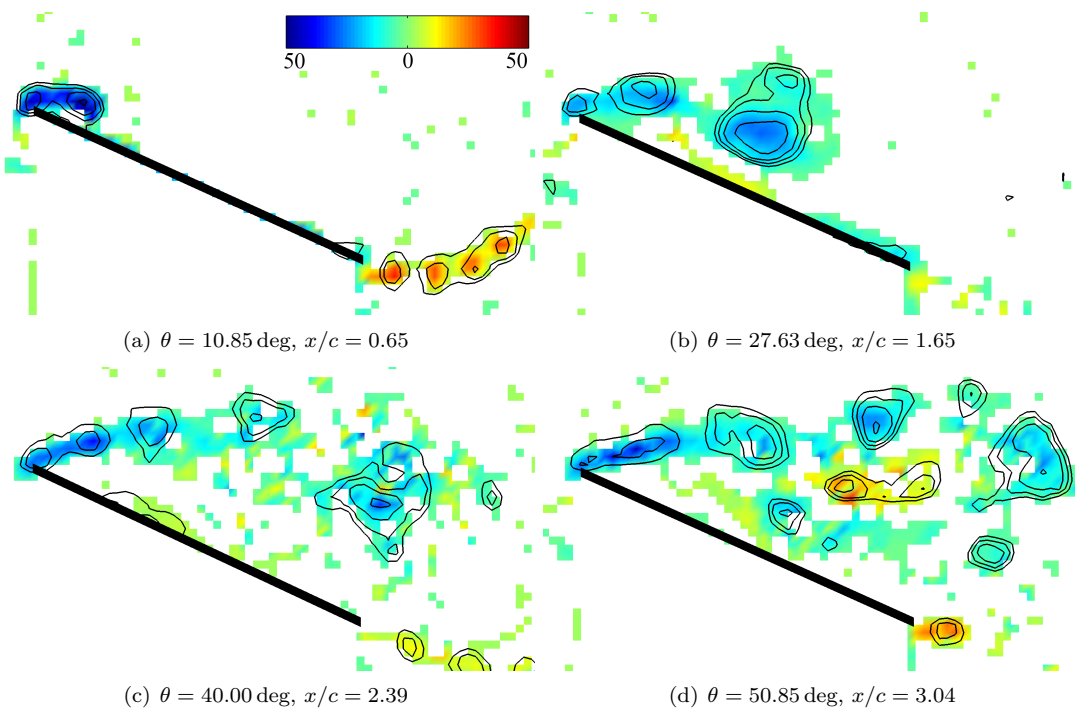


Figure 10. Normalized vorticity fields at $3/4$ span, $\text{Re} = 60,000$, $\alpha = 25 \text{ deg}$

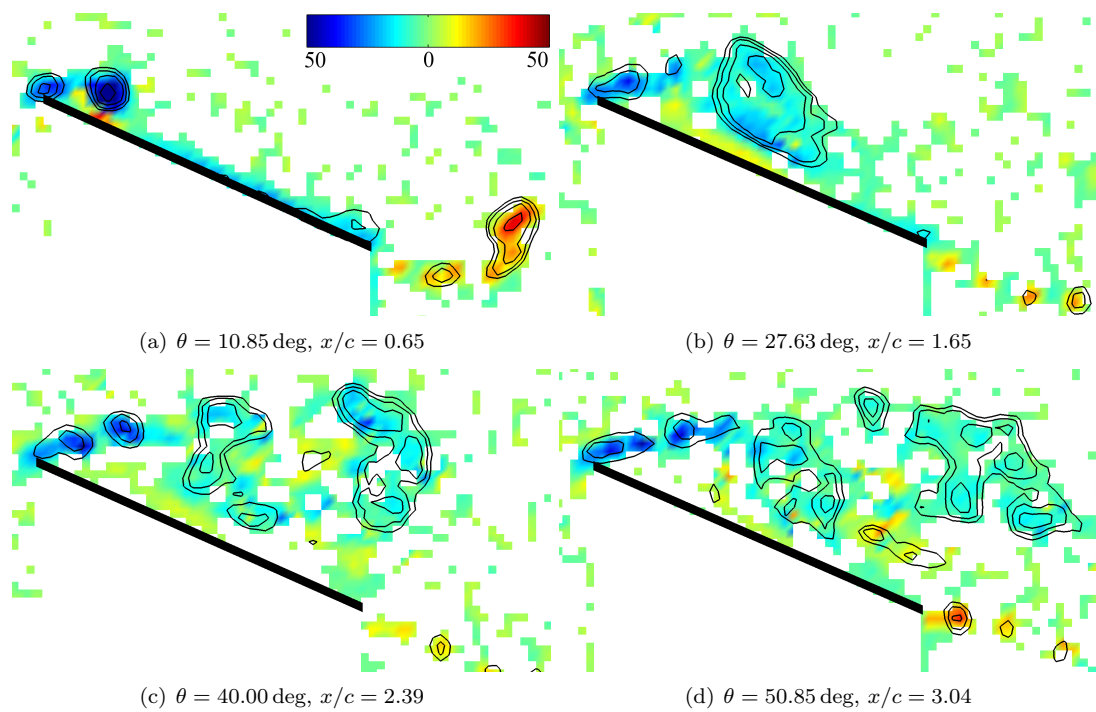


Figure 11. Normalized vorticity fields at 3/4 span, $Re = 30,000$, $\alpha = 25$ deg

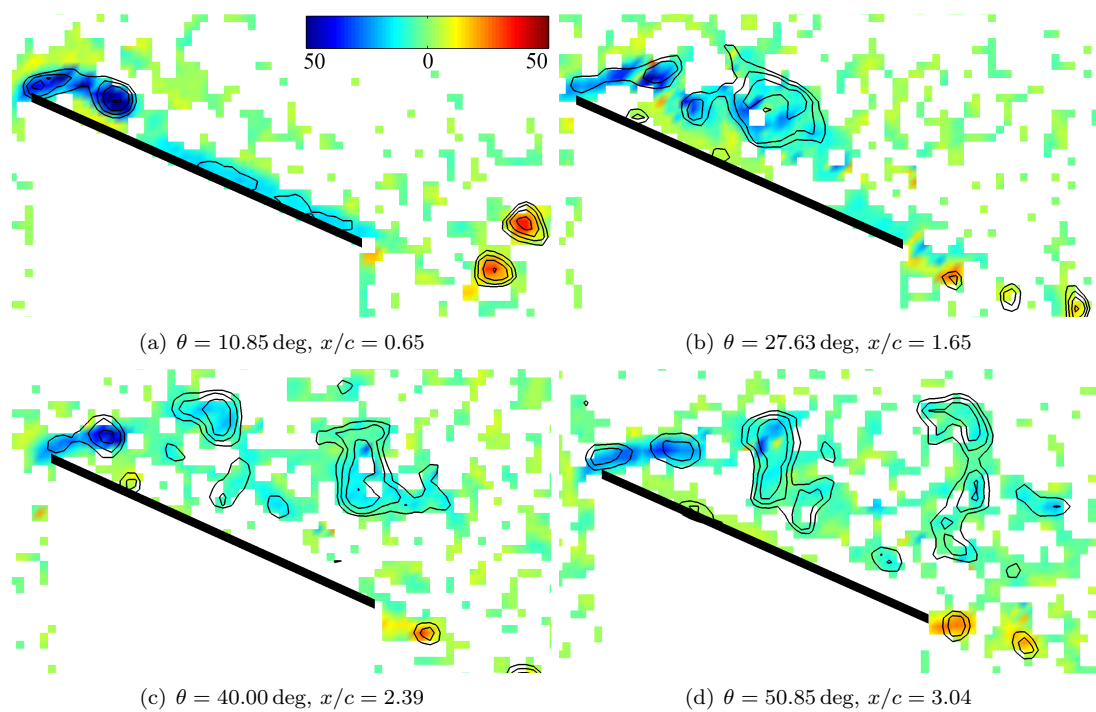


Figure 12. Normalized vorticity fields at 3/4 span, $Re = 10,000$, $\alpha = 25$ deg.

C. Unsteady Lift

The raw lift force as measured at Reynolds numbers 30,000 and 60,000 is given as a function of time in Figure 14. Also shown is the time-history of the wing's angular velocity. As mentioned previously, the wing kinematics are defined such that the wing reaches its target velocity when the 3/4 span plane has traveled 0.25 chord-lengths. The angular acceleration is thus lower at lower Reynolds numbers. At $Re = 30,000$ the wing acceleration is about half of that at $Re = 60,000$ and it takes a significantly longer time for the wing to reach the target steady state velocity. Despite the very different accelerations experienced by the wing, the build-up of lift force over time is similar at the two Reynolds numbers. The measured lift force is much larger at a Reynolds number of 60,000 than at 30,000, but the shape of the curves is similar. On one hand, this is not unexpected since previous experiments have suggested that at large accelerations the wing kinematics do not affect the development of the leading edge vortex.^{8,15} On the other hand, the wing is moving faster at the higher Reynolds number and produces a stronger vortex more quickly. In many flows the stronger vortex would shed sooner, but in this three-dimensional flow the spanwise velocity gradient (and resulting spanwise flow) is also affected and may help to keep the higher Reynolds number vortex attached for a longer time.

Looking at the unsteady lift in another reference frame, Figure 15 compares the lift coefficient at $Re = 30,000$ and 60,000 as a function of the distance traveled at the 3/4 span reference plane. The maximum lift coefficient is 2.27 ± 0.61 at $Re = 30,000$ and 1.98 ± 0.15 at $Re = 60,000$. The RMS error makes it difficult to say much about the differences in the magnitude of the lift coefficient, but it is clear that in this frame of reference the timing of the lift peak is different. Lift appears to grow more quickly (in terms of chord-lengths traveled) at $Re = 30,000$ and reaches a maximum earlier in the wing stroke (at a smaller value of x/c) than at $Re = 60,000$. This is consistent with the previous observation in Figure 13 that the leading edge vortex forms and sheds more quickly (after fewer chord-lengths traveled) at lower Reynolds numbers.

Figure 16 shows the lift coefficient (smoothed for clarity) as a function of chord-lengths traveled along with the vorticity field at $Re = 30,000$ at five points near the lift peak. The development of the leading edge vortex corresponds to the force history in the same way as suggested previously^{8,15} at $Re = 60,000$. Lift grows quickly from the start of the wing stroke as a leading edge vortex forms (a) and, for a short period of time, is attached to the wing. Lift values peak (b) just before the vortex sheds, and drop off as a second leading edge vortex forms (c). At $Re = 30,000$ the lift peak occurs at $x/c = 0.25$ whereas at $Re = 60,000$, the lift peak occurs at $x/c = 0.52$. Figure 17 shows the vorticity field at the $Re = 60,000$ lift peak, $x/c = 0.52$, for both Reynolds numbers. It is clear that the flow has developed more quickly at $Re = 30,000$, where two separate vortex cores are visible, than at $Re = 60,000$ where only a single vortex can be identified.

In order to quantify the development of the leading edge vortex, the normalized circulation $\Gamma^* = 2\Gamma/U_\infty c$ of the leading edge vortex was computed for each frame of the PIV data. Figure 18 shows Γ^* as a function of chord-lengths traveled for Reynolds numbers 10,000, 30,000, and 60,000. The vertical lines indicate the point at which the vortex breaks off of the wing as defined by the $|\gamma| = 0.8$ contour.[§] As observed in the vorticity

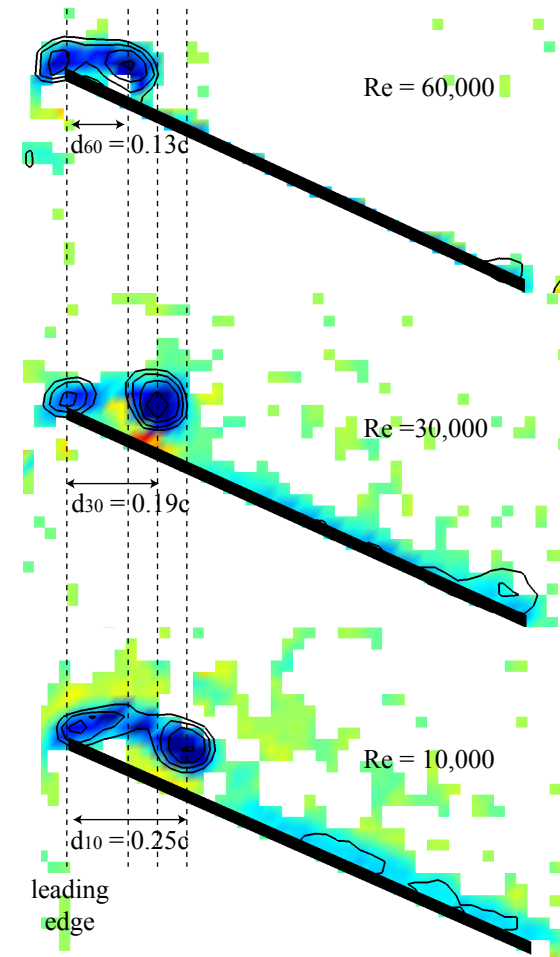


Figure 13. Normalized vorticity fields at 3/4 span, $\theta = 10.85$ deg, $x/c = 0.65$, $\alpha = 25$ deg.

[§]Note that the timing of the vortex break-off does not match the timing of the lift peak because the PIV data used to calculate Γ^* for these cases is of a relatively low resolution and the predicted vortex shedding point is very sensitive to this as discussed in Section 3.

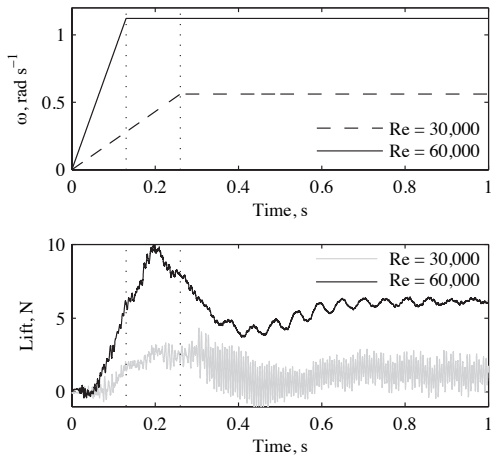


Figure 14. Raw lift force at $\alpha = 25$ deg as a function of time.

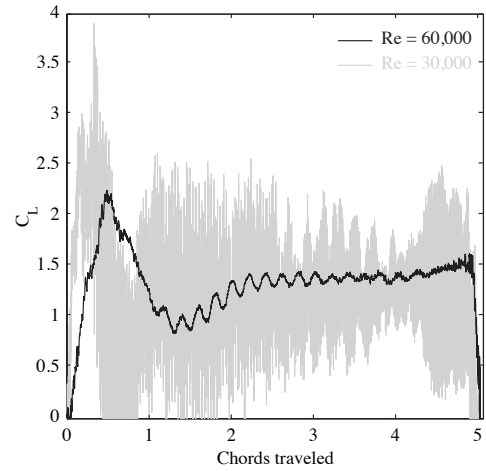


Figure 15. Raw lift coefficient at $\alpha = 25$ deg as a function of chords traveled.

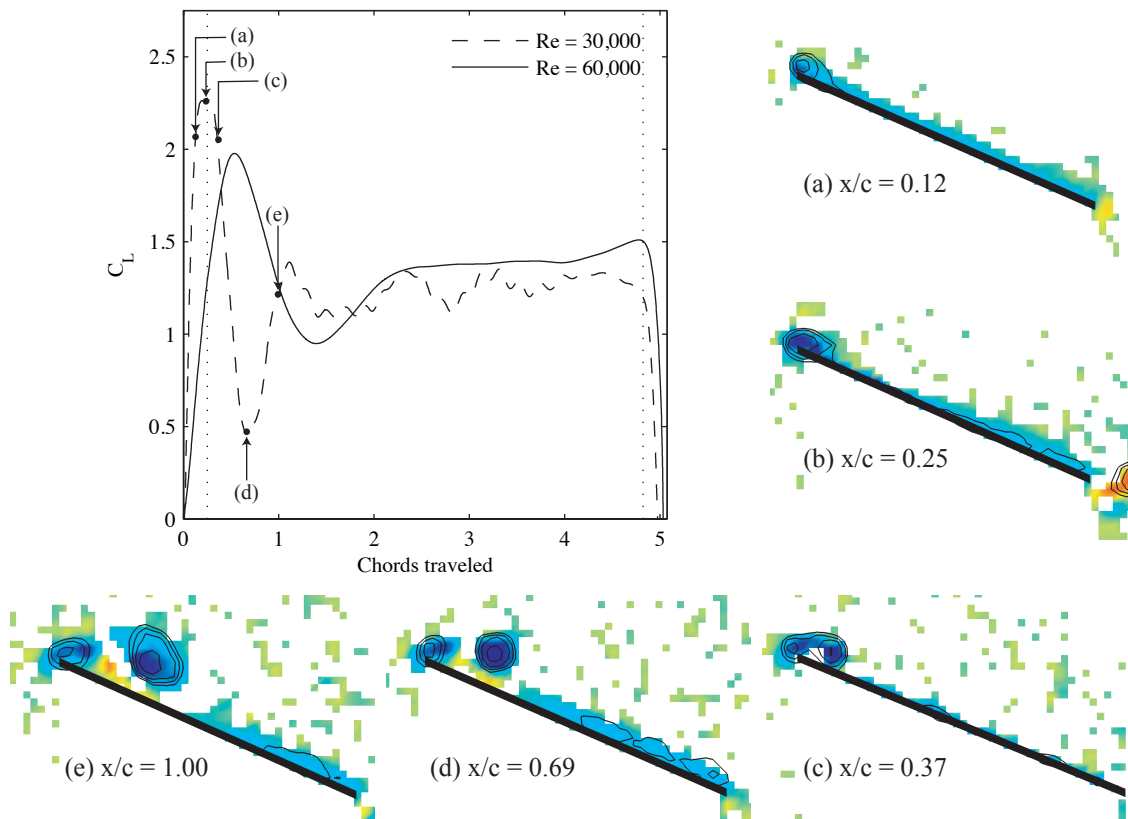


Figure 16. Lift coefficient and normalized vorticity fields at $3/4$ span, $\alpha = 25$ deg.

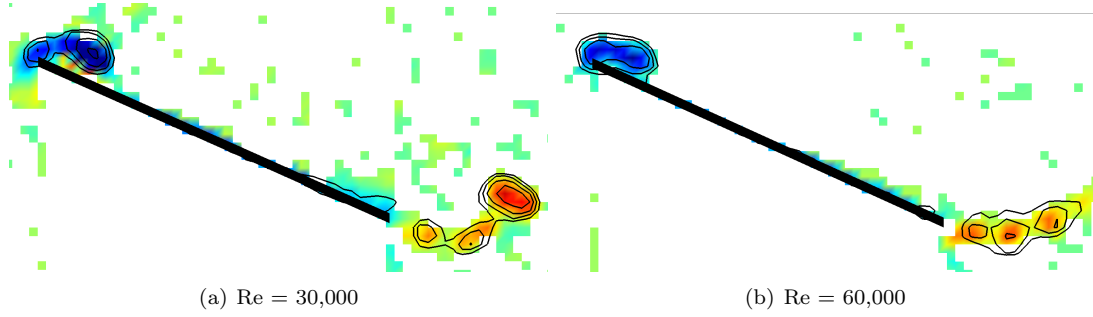


Figure 17. Normalized vorticity field at $x/c = 0.52$, $\alpha = 25$ deg.

fields shown previously, vortex break-off occurs significantly earlier at $Re = 30,000$ than at $Re = 60,000$ and even earlier still at $Re = 10,000$.

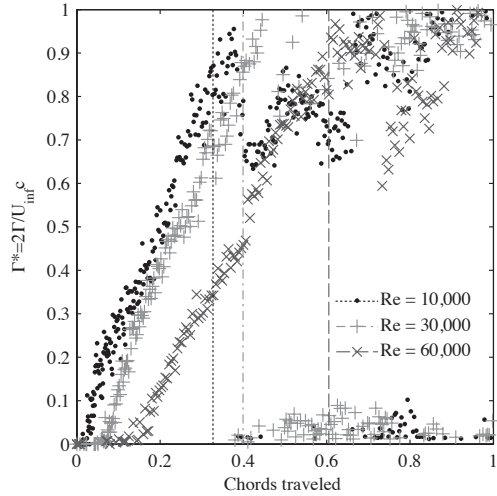


Figure 18. Leading edge vortex circulation at $3/4$ span, $\alpha = 25$ deg.

Another interesting observation can be made from Figure 18. At each Reynolds number, the leading edge vortex breaks off near $\Gamma^* \approx 0.88$. As discussed previously, the numerical value of Γ^* is sensitive to the path of integration, but the computation is repeatable and it is interesting that the break-off point appears to be related to this parameter. Predicting vortex break-off is a topic that is currently generating a lot of interest and many studies have tried to cast the current problem in a manner similar to the well-known formation time, traditionally applied to vortex rings generated via a cylinder and piston. The formation time of a vortex can be defined as¹⁶

$$\hat{T} = \frac{k\Gamma}{cU}$$

where k is the inverse of the vorticity flux, Γ is the instantaneous circulation of the vortex, c is the characteristic length taken to be the wing chord, and U is the characteristic velocity taken to be the target wing velocity U_∞ . Writing this in terms of the normalized circulation $\Gamma^* = 2\Gamma/U_\infty c$, the formation time becomes $\hat{T} = \Gamma^* k/2$, a function of the instantaneous normalized circulation and the vorticity flux which is in turn a function of the configuration of the vortex generator. For the current set of wing kinematics the vorticity flux is expected to increase with Reynolds number and thus k decreases as Reynolds number increases. If the vortex breaks off at the similar values of Γ^* for different Reynolds numbers, then it appears that the formation time of the initial leading edge vortex increases with Reynolds number between 10,000 and 60,000.

IV. Conclusions

Waving wing experiments were performed at Reynolds numbers 10,000, 30,000, and 60,000 in order to investigate the effect of Reynolds number on the development of the flow, in particular the leading edge vortex and the resulting lift forces. Instantaneous vorticity fields computed from PIV data reveal that the fundamental structure of the flow does not change significantly in the Reynolds number range tested, but the timing of the flow development does. The initial leading edge vortex appears to form more quickly (in the non-dimensional reference frame of chord-lengths traveled) at lower Reynolds numbers. Force measurements reveal that the maximum lift occurs earlier in the wing stroke at lower Reynolds numbers, consistent with the earlier development of the leading edge vortex.

V. Acknowledgements

The authors gratefully acknowledge financial support provided by the Air Force Office of Scientific, Air Force Material Command, USAF under EOARD Grant FA 8655-07-1-3082 and the National Science Foundation. The U.S. government is authorized to reproduce and distribute reprints for Government purpose notwithstanding any copyright notation thereon. The views and conclusions contained herein are those of the author and should not be interpreted as necessarily representing the official policies or endorsements, either expressed or implied, of the Air Force Office of Scientific Research or the U.S. Government.

References

- ¹Ellington, C. P., van den Berg, C., Willmott, A. P., and Thomas, A. L. R., "Leading-edge vortices in insect flight," *Nature*, Vol. 384, No. 6610, December 1996, pp. 626–630.
- ²Birch, J. M., Dickson, W. B., and Dickinson, M. H., "Force Production and Flow Structure of the Leading Edge Vortex on Flapping Wings at High and Low Reynolds Numbers," *Journal of Experimental Biology*, Vol. 207, No. 7, 2004, pp. 1063–1072.
- ³van den Berg, C. and Ellington, C. P., "The Vortex Wake of a "Hovering" Model Hawkmoth," *Philosophical Transactions of the Royal Society of London, Series B, Biological Sciences*, Vol. 352, No. 1351, 1997, pp. 317–328.
- ⁴van den Berg, C. and Ellington, C. P., "The Three-Dimensional Leading-Edge Vortex of a "Hovering" Model Hawkmoth," *Philosophical Transactions of the Royal Society of London, Series B, Biological Sciences*, Vol. 352, No. 1351, 1997, pp. 329–340.
- ⁵Usherwood, J. R. and Ellington, C. P., "The Aerodynamics of Revolving Wings: I. Model Hawkmoth Wings," *Journal of Experimental Biology*, Vol. 205, No. 11, 2002, pp. 1547–1564.
- ⁶Tarascio, M. J., Ramasamy, M., Chopra, I., and Leishman, J. G., "Flow Visualization of Micro Air Vehicle Scaled Insect-Based Flapping Wings," *Journal of Aircraft*, Vol. 42, No. 2, March-April 2005, pp. 385–390.
- ⁷Lentink, D. and Dickinson, M. H., "Rotational Accelerations Stabilize Leading Edge Vortices on Revolving Fly Wings," *Journal of Experimental Biology*, Vol. 212, April 2009, pp. 2705–2719.
- ⁸Jones, A. R. and Babinsky, H., "Unsteady Lift Generation on Rotating Wings at Low Reynolds Numbers," *Journal of Aircraft*, Vol. 47, No. 3, 2010, pp. 1013–1021.
- ⁹Maxworthy, T., "Experiments on the Weis-Fogh Mechanism of Lift Generation by Insects in Hovering Flight, I. Dynamics of the 'fling,'" *Journal of Fluid Mechanics*, Vol. 93, No. 1, July 1979, pp. 47–63.
- ¹⁰Birch, J. M. and Dickinson, M. H., "Spanwise flow and the attachment of the leading-edge vortex on insect wings," *Nature*, Vol. 412, No. 6848, August 2001, pp. 729–733.
- ¹¹Jones, A. R., *Unsteady Low Reynolds Number Aerodynamics of a Waving Wing*, Phd, University of Cambridge, May 2010.
- ¹²Jeong, J. and Hussain, F., "On the Identification of a Vortex," *Journal of Fluid Mechanics*, Vol. 285, February 1995, pp. 69–94.
- ¹³Raffel, M., Willert, C. E., and Kompenhans, J., *Particle Image Velocimetry: A Practical Guide*, Springer, 1998.
- ¹⁴Graftieaux, L., Michard, M., and Grosjean, N., "Combining PIV, POD and Vortex Identification Algorithms for the Study of Unsteady Turbulent Swirling Flows," *Measurement Science and Technology*, Vol. 12, No. 9, August 2001, pp. 1422–1429.
- ¹⁵Jones, A. R. and Babinsky, H., "Three-Dimensional Effects on a Waving Wing," *48th AIAA Aerospace Sciences Meeting and Exhibit*, AIAA 2010-0551, Orlando, FL, 4-7 January 2010.
- ¹⁶Dabiri, J. O., "Optimal Vortex Formation as a Unifying Principle in Biological Propulsion," *Annual Review of Fluid Mechanics*, Vol. 41, No. 1, 2009, pp. 17–33.